POLITECNICO DI TORINO
Repository ISTITUZIONALE

The dual wavelength ratio Knee: A signature of multiple scattering in airborne Ku-Ka observations

Original
The dual wavelength ratio Knee: A signature of multiple scattering in airborne Ku-Ka observations / Battaglia, A.; Tanelli, S.; Heymsfield, G. M.; Tian, L.. - In: JOURNAL OF APPLIED METEOROLOGY AND CLIMATOLOGY. - ISSN 1558-8424. - 53:7(2014), pp. 1790-1808. [10.1175/JAMC-D-13-0341.1]

Availability:
This version is available at: 11583/2808964 since: 2020-04-05T20:36:17Z

Publisher:
American Meteorological Society

Published
DOI:10.1175/JAMC-D-13-0341.1

Terms of use:

This article is made available under terms and conditions as specified in the corresponding bibliographic description in the repository

Publisher copyright

(Article begins on next page)

21 December 2024

The Dual Wavelength Ratio Knee: A Signature of Multiple Scattering in Airborne Ku–Ka Observations

ALESSANDRO BATTAGLIA*

Department of Physics and Astronomy, University of Leicester, Leicester, United Kingdom

SIMONE TANELLI

Jet Propulsion Laboratory, California Institute of Technology, Pasadena, California

GERALD M. HEYMSFIELD

NASA Goddard Space Flight Center, Greenbelt, Maryland

LIN TIAN

NASA Goddard Space Flight Center, Greenbelt, and Morgan State University, Baltimore, Maryland

(Manuscript received 8 November 2013, in final form 5 March 2014)

ABSTRACT

Deep convective systems observed by the High Altitude Imaging Wind and Rain Airborne Profiler (HIWRAP) radar during the 2011 Midlatitude Continental Convective Clouds Experiment (MC3E) field campaign in Oklahoma provide the first evidence of multiple-scattering effects simultaneously at Ku and Ka band. One feature is novel and noteworthy: often, in correspondence to shafts with strong convection and when moving from the top of the cloud downward, the dual wavelength ratio (DWR) first increases as usual in Ku–Ka-band observations, but then it reaches a maximum and after that point it steadily decreases all the way to the surface, forming what will be hereinafter referred to as a *knee*. This DWR knee cannot be reproduced by single-scattering theory under almost any plausible cloud microphysical profile. On the other hand, it is explained straightforwardly with the help of multiple-scattering theory when simulations involving hail-bearing convective cores with large horizontal extents are performed. The DWR reduction in the lower troposphere (i.e., DWR increasing with altitude) is interpreted as the result of multiple-scattering pulse stretching caused by the highly diffusive hail layer positioned high up in the atmosphere, with Ka multiple scattering typically exceeding that occurring in the Ku channel. Since the effects of multiple scattering increase with increasing footprint size, if multiple-scattering effects are present in the aircraft measurements, they are likely to be more pronounced in the spaceborne dual-frequency Ku–Ka radar observations, envisaged for the NASA–Japan Aerospace Exploration Agency (JAXA) Global Precipitation Measurement (GPM) Mission, launched in February 2014. This notional study supports the idea that DWR knees will be observed by the GPM radar when overflying high-density ice shafts embedded in large convective systems and suggests that their explanation must not be sought in differential attenuation or differential Mie effects but via multiple-scattering effects.

1. Introduction

The launch of the National Aeronautics and Space Administration (NASA)–Japan Aerospace Exploration Agency (JAXA) Global Precipitation Measurement (GPM) Mission with its dual-frequency (Ku and Ka band) precipitation radar (DPR) in February 2014 is expected to provide a breakthrough in the observation and monitoring of global precipitation (Hou et al. 2014). The GPM radar will provide the first-ever collocated dual-frequency profiles of precipitation; moreover, although the Ku frequency is heritage from the still ongoing Tropical Rainfall Measuring Mission (TRMM; Kummerow et al.

* *Corresponding author address:* Alessandro Battaglia, Dept. of Physics and Astronomy, University of Leicester, University Road, Leicester LE1 7RH, United Kingdom.
E-mail: ab474@le.ac.uk

DOI: 10.1175/JAMC-D-13-0341.1

© 2014 American Meteorological Society

1998), the Ka frequency will represent an absolute novelty for cloud and precipitation radar studies from space.

An area where the DPR could shed new light is in the characterization of deep convection. Single-frequency radars such as the TRMM Ku precipitation radar or the *CloudSat* W-band cloud profiling radar (CPR; Tanelli et al. 2008) have contributed to a better understanding of deep convective systems (e.g., Liu et al. 2007; Luo et al. 2008), but the identification and quantification of hydrometeor characteristics for such systems is typically difficult. In fact, the likely presence of large particles can produce significant Mie and attenuation effects, which are difficult to identify and disentangle with single-frequency observations. In addition to that, because large ice particles are typically very good scatterers, regions of deep convection may become sources of multiple scattering (MS), a phenomenon that has been extensively studied in recent years in relationship to *CloudSat* W-band radar observations (Kobayashi et al. 2005; Battaglia et al. 2007, 2008, 2010; Mitrescu et al. 2010). Battaglia et al. (2011) pointed out that for deep convective cores only the upper part of *CloudSat* CPR profiles can be confidently interpreted with single-scattering (SS) theory, that is, by assuming that the received power comes from radiation that has directly traveled from the radar transmitter to the scatterer and then backscattered by an hydrometeor target to the radar receiver, possibly being attenuated within the two-way path. MS can occur at frequencies below the W band as well. In general, for strongly attenuating hydrometeors and especially in the presence of large ice particles—for which most of the attenuation is caused by scattering processes—the radar equation must include contributions from higher orders of scattering. Errors caused by MS effects are expected to be large when the transport mean-free path becomes comparable with the instrument footprint as determined by the antenna beamwidth and the platform altitude (Battaglia et al. 2010). Past simulation studies (Battaglia et al. 2006a,b) and a recent review of TRMM datasets (S. Tanelli 2013, unpublished presentation at Precipitation Measuring Mission Science Team Meeting) suggest that such effects could indeed occur also for GPM observations of convective cores. In this work we document evidence of MS from airborne measurements at Ku and Ka acquired by the High Altitude Imaging Wind and Rain Airborne Profiler (HIWRAP) radar on board the NASA ER-2 airplane when overflying deep convective systems during the Midlatitude Continental Convective Clouds Experiment (MC3E) campaign (Heymsfield et al. 2013). As previously used in Tian et al. (2002), in order to add additional constraints to the problem, the S-band KOUN (Norman, Oklahoma) ground-based radar data have been mapped from RHI scan radar coordinates into latitude–longitude coordinates of the ER-2 flight line.

Although this case study can be considered as an extreme weather scenario, some of the signatures reported are particularly instructive for a correct interpretation of GPM observations in convective cores. Section 2 presents the airborne radar observations, their salient features, and the difficulties in explaining them within a SS approach; section 3 describes how to reconcile radar observations with theory by accounting for MS effects. The potential impact for GPM observations is discussed in section 4. Conclusions are then presented in section 5.

2. HIWRAP dual-frequency airborne observations of convective towers

HIWRAP, a new dual-frequency (Ku and Ka band) nadir-pointing Doppler radar on board the high-altitude (above 18 km) ER-2 airplane, has collected data over severe thunderstorms in Oklahoma and Kansas during MC3E. Two ER-2 flights and several severe thunderstorm overpasses on 23–24 May 2011 have been documented in Heymsfield et al. (2013). A comprehensive description of the HIWRAP instrument and of the associated signal processing is reported in the same paper and references therein. Here we focus on the storm denoted as C1 by Heymsfield et al. (2013) and specifically to a convective tower observed between 0121 and 0126 UTC 24 May 2011 [Figs. 9 and 10 in Heymsfield et al. (2013)]. The reflectivity profiles measured by HIWRAP at Ku and Ka are here reported in Figs. 1a and 1b [note that our x axis reference is shifted by roughly 18 km relative to Figs. 9 and 10 in Heymsfield et al. (2013) in order to better visualize the whole convective cell] and clearly show a deep convective core towering up to more than 16 km and with an horizontal extension exceeding 20 km corresponding to along-track distances between 12 and 38 km. The cell is producing a lot of attenuation both at Ka and at Ku, with the Ka signal completely attenuated for heights below 4 km at the center of the core. The marked convective nature of the system is confirmed by the Ku Doppler velocity (Fig. 1d) with updrafts (downdrafts) exceeding 40 m s^{-1} (-30 m s^{-1}). Ground-based reports and the polarimetric signatures observed by the KOUN S-band polarimetric radar located at Norman suggest the presence of large hailstones in the cell [see discussion in Heymsfield et al. (2013)]. Collocated reflectivities of the S-band radar exceed 50 dBZ within the cell for all altitudes below 10 km and in several regions exceed 60 dBZ with a slight tilting from the bottom right to the top left of the core of maximum reflectivity, where hail is likely present [top-left panel in Fig. 9 in Heymsfield et al.

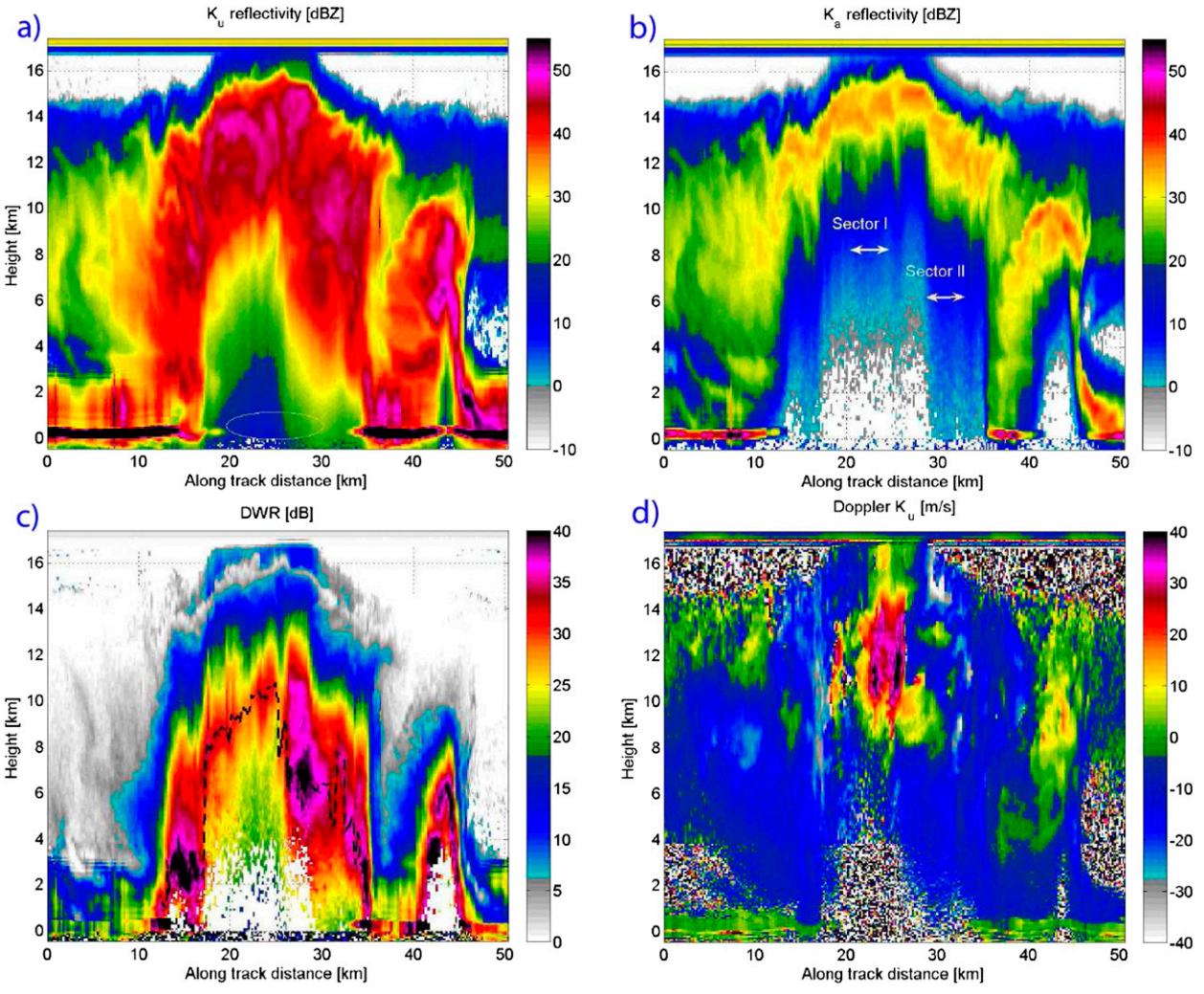

FIG. 1. HIWRAP (a) Ku and (b) Ka vertical profiles of reflectivities for a convective cell observed during the MC3 campaign. Also shown are (c) DWR and (d) Ku Doppler velocity for the convective cell considered in this study. The dashed black line in (c) indicates the position of the DWR knee.

(2013)]. Because of the clear transition in the reflectivity profile structure occurring around an along-track distance of 27 km, in this paper we consider and discuss two distinct sectors of the cell centered at 24 and around 31 km (see double arrows in Fig. 1b).

a. Salient features in the observed profiles

The convective tower features some interesting aspects. Two are germane to this study:

1) the disappearance in the Ku channel of a clear discontinuity in the reflectivity profile in correspondence to the surface—which is typically caused by the predominance of the surface on the hydrometeor return—for along-track distances between 20 and 32 km (see dashed ellipse in Fig. 1a) (feature 1) and
2) the anomalous sloping of the Ku (relative to the Ka) reflectivity profiles below a certain height (identified by the dashed black line in Fig. 1c) with vertical reflectivity gradient at Ka, $dZ_{\mathrm{att,ka}}/dz$, smaller than or comparable with that at Ku, $dZ_{\mathrm{att,ku}}/dz$ (feature 2), where $Z_{\mathrm{att},f}$ is the frequency-dependent attenuated reflectivity factor.

To better visualize the latter feature, it is useful to introduce the dual wavelength ratio (DWR), defined as the ratio of reflectivity factors from the two collocated HIWRAP channels, or in logarithmic units as

$$\mathrm{DWR}(z)\ (\mathrm{dB}) \equiv Z_{\mathrm{att,Ku}}(z)\ (\mathrm{dB}Z) - Z_{\mathrm{att,Ka}}(z)\ (\mathrm{dB}Z). \tag{1}$$

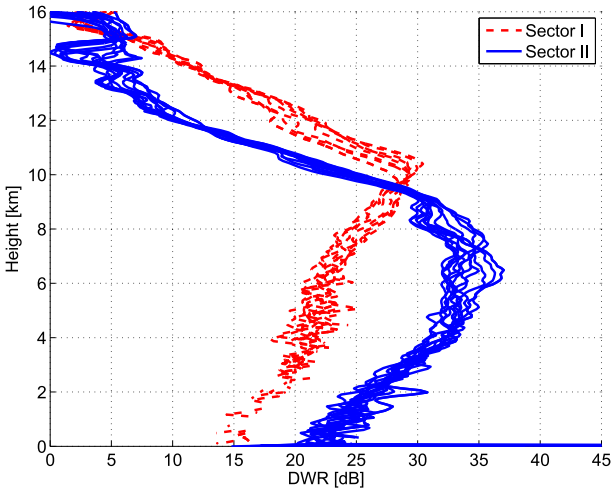

FIG. 2. The DWR knee as derived from HIWRAP measurements in sectors I and II.

Feature 2 is reflected into the presence of a knee in the DWR as demonstrated in Fig. 2. In all the DWR vertical profiles corresponding to the convective cell the DWR first reaches a maximum (whose position is marked by the dashed black line in Fig. 1c) and then decreases. It is important to note the considerable size of the knee both in terms of extent (height) and depth (dB excursion). For instance, for sector I (II) the leg below the knee stretches for 8 km (4–5 km) with a decrease of about 10 dB (15 dB). One last important detail in the observed profiles of $Z_{\rm att}$ is that below the knee the curve is either generally flat or concave (i.e., generally $dZ_{\rm att}/dh$ and $d^2Z_{\rm att}/dh^2$ are nonnegative), and it results in remarkably small slopes at the range corresponding to the surface (i.e., $<2\,{\rm dB\,km^{-1}}$). As we will see hereinafter these are key features supporting the MS hypothesis (i.e., only MS can make such long-deep knees).

It is worth noting that the DWR knee was not a *rara avis* in the HIWRAP dataset during the MC3E campaign but has been observed several times in correspondence of deep convective cores.

b. *Difficulties in interpretation of the profiles with SS theory*

It is extremely difficult to explain the disappearance of the surface return at Ku (feature 1) in a SS scenario. Based on the TRMM nadir surface return dataset for Oklahoma (in a region immediately south of the ER-2 overflight location, but with similar land cover) we can assume the surface normalized cross section (Meneghini and Kozu 1990) σ^0 to be certainly above 0 dB with typical values between 4 and 17 dB (Durden et al. 2012). Wet surface σ^0s are likely to exceed these values.

With $\sigma^0 = 0\,{\rm dB}$ we do expect a surface return at $\approx$64 dBZ for the HIWRAP Ku band (vertical resolution of 300 m). Since the observed $Z_{\rm att,Ku}$ at the surface range is about 14 dBZ, it follows that we must have a total two-way attenuation at Ku of at least 50 dB, and this indirectly implies the presence of targets with reflectivities above 64 dBZ close to the surface but not characterized by a strong Ku and Ka attenuation (since the observed slope of $Z_{\rm att,Ku}$ is only of $2\,{\rm dB\,km^{-1}}$ for 6 km around the surface range; see Fig. 10a later on). Of course we can exclude immediately rain or wet hail, because the increase in refractive index further increases the ratio of specific attenuation over backscatter. Also, we can exclude low-density ice both on climatological grounds and, most important, on the simple fact that it would require, for example, more than $100\,{\rm g\,m^{-3}}$ of $0.4\,{\rm g\,cm^{-3}}$ graupel even with $D_m = 5$ mm to achieve the 65-dBZ mark (see magenta line in the top-right panel of Fig. 3). The only plausible SS explanation for feature 1 in the HIWRAP observations could have been very large hailstones (e.g., larger than 2.5 cm in diameter). But even dry hail—and 50-mm hail was indeed observed at the surface with these storm—cannot reproduce observations. By rescaling accordingly to the mass content the backscattering and attenuation coefficients shown in Fig. 3b, $10\,{\rm g\,m^{-3}}$ of hailstones between 30 and 40 mm could produce a Ku backscattering signal of approximately 65 dBZ (i.e., 10×55 dBZ). This would produce at least $4\,{\rm dB\,km^{-1}}$ of attenuation [the attenuation coefficient per unit mass is $>0.4\,{\rm dB\,km^{-1}\,(g\,m^{-3})^{-1}}$; see Fig. 3a], which is more than in the observed profile. Moreover, collocated S-band observations never exceeded 65 dBZ whereas such hailstones should result in reflectivities exceeding 77 dBZ at S band because of the S–Ku Mie differential response (larger than 12 dB for $D_m > 1$ cm).

Similarly, it is very complicated in an SS scenario to produce knees in DWR with the bottom part of the leg sloping down with gradients of $2\,{\rm dB\,km^{-1}}$ or less for thickness of several kilometers. In fact, *in the SS assumption* the attenuated reflectivity factor at a given frequency f and at height z can be expanded as

$$Z_{{\rm att},f}(z) = Z_{{\rm eff},f}(z) - 2\int_z^{H_{\rm plane}} \alpha_f(s)\,ds, \qquad (2)$$

where α and $Z_{\rm eff}$ are the one-way specific attenuation (which accounts for attenuation by gases and hydrometeors) and the effective reflectivity, respectively; $H_{\rm plane}$ is the height of the airplane (about 20 km for this case study). Therefore the DWR can then be expressed as

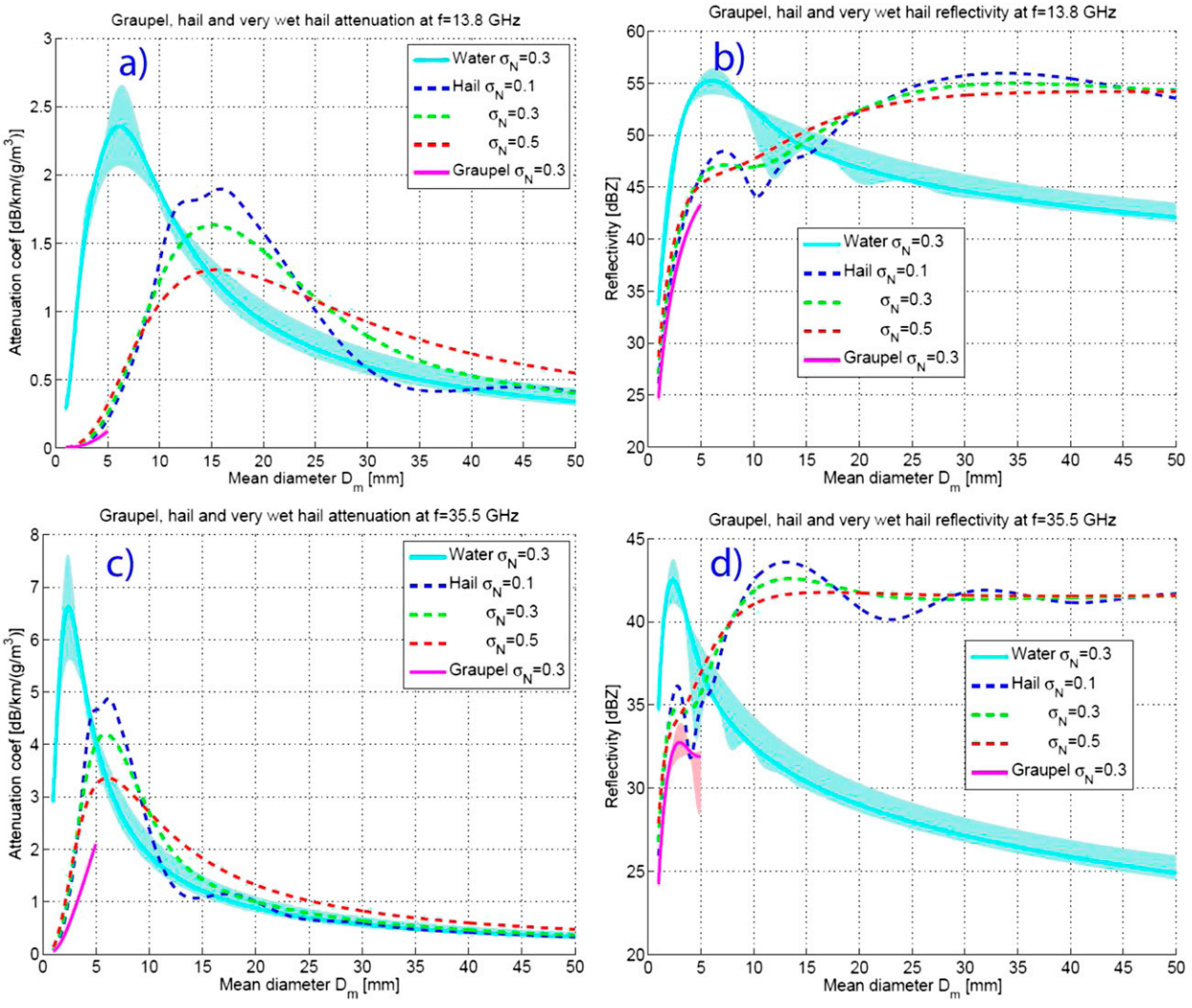

FIG. 3. (left) Attenuation coefficients per unit mass and (right) backscattering coefficients for HWC = $1\,\mathrm{g\,m^{-3}}$ at (a),(b) Ku and (c),(d) Ka bands. A value of $0.9\,\mathrm{g\,cm^{-3}}$ is assumed for the hail density. Results are plotted for three gamma particle size distributions as a function of the mass-weighted mean diameter D_m with different normalized widths $\sigma_N \equiv \sqrt{1/(\mu+4)}$ with $\mu = 1/\sigma_N^2 - 4$ being the shape parameter of the gamma distribution. Rain (indicated as water in the legend) is fictitiously plotted also for large D_m to simulate the effect of melting hailstones with a thick water coating. The shading in rain and graupel accounts for the variability of σ_N between 0.1 and 0.5.

$$\mathrm{DWR}(z) = \overbrace{\underbrace{Z_{\mathrm{eff,Ku}}(z) - Z_{\mathrm{eff,Ka}}(z)}_{\text{Mie effect}}}^{\mathrm{DWR_{eff}}} - \underbrace{2\int_z^{H_{\mathrm{plane}}} [\alpha_{\mathrm{Ku}}(s) - \alpha_{\mathrm{Ka}}(s)]\,ds}_{\text{attenuation effect}}. \qquad (3)$$

$$\frac{d\mathrm{DWR}(z)}{dz} = \underbrace{\frac{d\mathrm{DWR_{eff}}(z)}{dz}}_{\text{differential Mie}} + \underbrace{2[\alpha_{\mathrm{Ku}}(z) - \alpha_{\mathrm{Ka}}(z)]}_{\text{differential attenuation}} = \frac{d\mathrm{DWR_{eff}}}{dD_m}\frac{dD_m}{dz} + 2[\alpha_{\mathrm{Ku}}(z) - \alpha_{\mathrm{Ka}}(z)]. \qquad (4)$$

That is, in the "SS world" the DWR is the result both of differential effective reflectivities (Mie effects) and differential attenuation effects. Taking the vertical derivative of Eq. (3) we get

As a result a vertical change in DWR can be produced in SS theory 1) by differential effective reflectivity or Mie effects [first term in Eq. (4)] due to a vertical change in the hydrometeor size, 2) by differential attenuation

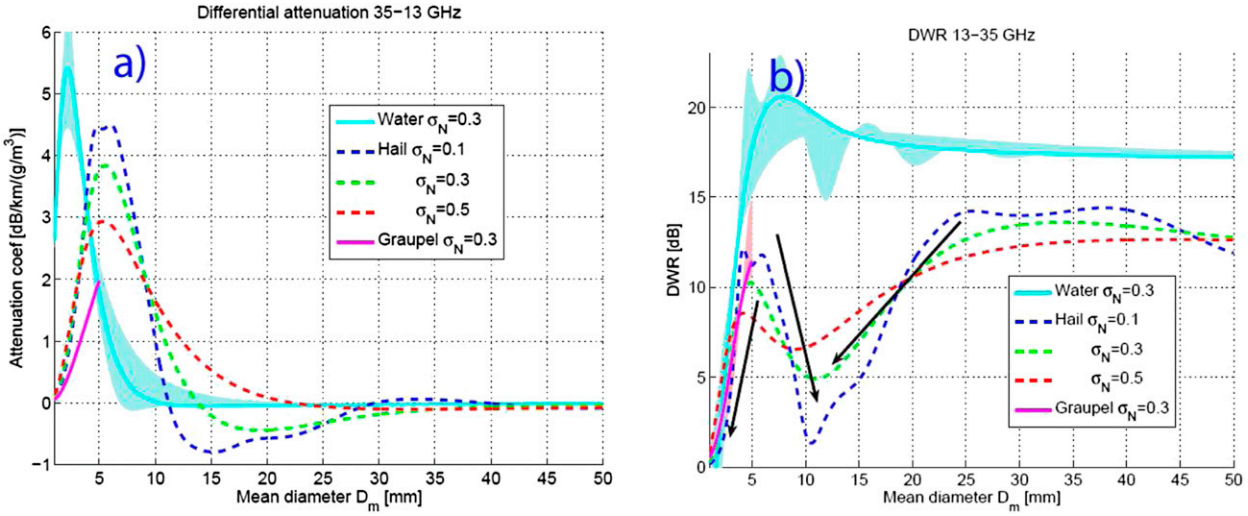

FIG. 4. (a) Differential attenuation and (b) differential reflectivity for the HIWRAP system for graupel, rain, and hail as a function of the mass-weighted mean diameter for exponential size distributions. Rain (labeled as water) is also fictitiously plotted for large D_m to simulate the effect of melting hailstones with a thick water coating.

effects [second term in Eq. (4)], or 3) by a combination of the previous two. Naively it may be considered true that attenuation at Ka is always exceeding the attenuation at Ku band for all hydrometeor types possibly present in our atmosphere. Differential attenuation effects are then expected to produce a DWR decrease with increasing height in space or airborne observations; thus they are at odds with the DWR knee signature. While such an assumption is true for raindrops, graupel, and ice crystals, it is not always correct for dry hail particles. Figure 4a [see also Fig. 14 in Heymsfield et al. (2013)] shows that there are ranges of hailstone diameters where attenuation at Ku is actually larger than attenuation at Ka! When hail size distributions are considered this property is preserved for very narrow gamma distributions (i.e., with a normalized width $\sigma_N = 0.1$), whereas it tends to be smoothed out for exponential size distributions ($\sigma_N = 0.5$). Exponential and gamma size distributions with σ_N in the range between 0.2 and 0.5 (i.e., $0 < \mu < 21$) values are also used in cloud-resolving modeling (Loftus 2012; Ryzhkov et al. 2013). Therefore, in principle, the presence of such large hailstones could generate a DWR that is increasing with height. However, such hailstone content is also associated with specific attenuations at Ku band that exceed the observed slope of reflectivity (determined by the two-way attenuation) by a factor of 2 or more. In other words, this regime could possibly reproduce the observed DWR curve, but not the Z_{att} curves at its origins.

Differential Ku–Ka Mie effects are more difficult to tackle. While for ice crystals, graupel, and raindrops DWR tends to increase with increasing particle size (Matrosov 1993; Kneifel et al. 2011) [with the exception of a small (<2 dB) decrease for raindrops with mass-weighted mean diameter increasing up to 1.2–1.5 mm; Matrosov et al. 2005], the situation is much more complicated when dealing with large hailstones, which are deep in the Mie-scattering regime. The arrows in Fig. 4b show directions that are compatible with a DWR increase with height: a decrease of characteristic size from 4 mm downward, an increase of size from 5 to 10 mm, or a decrease in size for particles with radii between 10 and 30 mm. Further investigation has proven that hailstones with mass-weighted mean diameters D_m within the sweet spot between 12 and 25 mm can provide DWR signals similar to those observed (and compatible with the reflectivity vertical gradients as well), although it is quite hard to produce such features for thick layers [~(4–5) km] and with large decrease (>10 dB) in the DWR amplitude as those observed. For instance, if we assume starting from hailstones with D_m of the order of 25 mm at the knee, a decrease in size will roughly produce a variation in DWR_{eff} on the order of 1 dB mm^{-1} (see slope of the black line on the far right in Fig. 4b). Values of observed $d\text{DWR}(z)/dz$ range up to 3–4 dB km^{-1} below the knee. This would require a decrease in D_m below the knee of the order of 3–4 mm km^{-1} [see expression on the right-hand side of Eq. (4)], which would reduce the size of hailstones to less than 1 cm by the zero isotherm. But the collocated S-band measurements (e.g., Figs. 10 and 11) are still well above 50 dBZ. Given these constraints, the resulting amount of hail (certainly exceeding 1 g m^{-3}) would produce large specific attenuations (especially at Ka), not reflected at all in

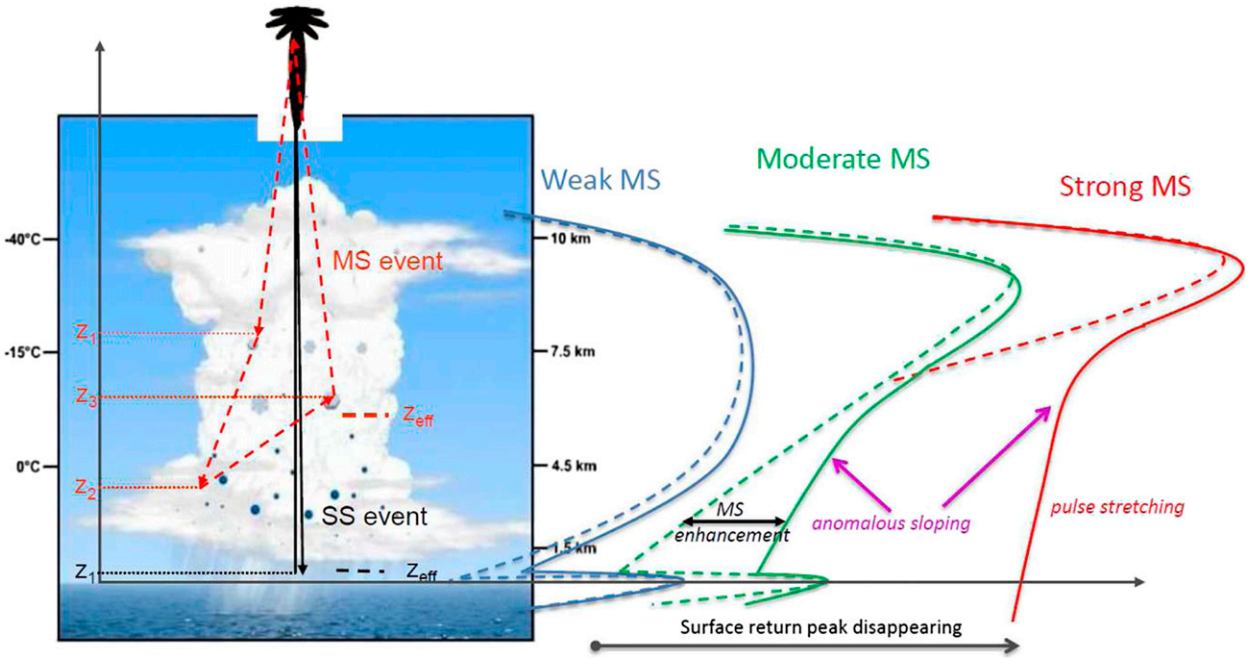

FIG. 5. (left) A cumulonimbus cloud as would be observed from an airborne platform. Contributions to the same apparent range (corresponding to the lower rainy region) from an SS and a three-order-of-scattering event generated within the ice portion of the cloud. Note the difference in the effective height between the two events (see text for details). (right) Conceptual model of vertical reflectivity profiles with increasing levels of MS effects. Continuous (dashed) lines correspond to MS (SS) profiles.

the shape of the observed Z_{att}. In general, besides considerations regarding the realism of a microphysical environment where such dramatic changes happen systematically (note that many profiles exhibit this behavior across several kilometers), no solution could be found in the typical scattering tables that reconciles the absolute levels as well as their slopes of the Ku-, Ka-, and S-band data.

3. MS framework

Instead of having to rely on extremely complicated (and somewhat unrealistic) configurations, the MS theory can explain the presence of the two features relatively easily. While MS effects have been accounted for in the interpretation of atmospheric lidar returns by the lidar community for a long time, historically they have been neglected when interpreting radar echoes. The only exception was represented by two- or three-body scattering features, like hail flares and mirror images [see Battaglia et al. (2010) and references therein]. The situation has radically changed with the launch of the W-band *CloudSat* radar. When moving from centimeter to millimeter wavelengths, the associated increase in the extinction coefficient and in the SS albedos of hydrometeors, as well as the change of their scattering phase functions toward more forward peaked ones, has enhanced the significance of higher orders of scattering in the radar echo. In scattering media where the mean scattering radiation length—equal to the inverse of the scattering coefficient—becomes comparable with the radar footprint, the radar signal cannot be interpreted based on the SS approximation (Kobayashi et al. 2007; Battaglia et al. 2010). Differently from what has already been experienced in lidar observations, at millimeter wavelengths hydrometeors diffuse radiation with a predominance of wide- versus small-angle scattering events (Hogan and Battaglia 2008). As a result, MS events may sense a completely different atmosphere than SS events corresponding to the same apparent range as demonstrated in the example provided on the left side of Fig. 5. The overall effect is to "stretch" the effect of a scattering layer beyond the actual range of the layer itself and to affect the signal coming from ranges longer than those associated to the layer itself, a phenomenon sometimes referred to as "pulse stretching," which can be seen as an analog of reverberation in acoustics (and since time is range in the radar equation, reverberation equates to profiles stretched away from the radar, or downward for nadir-looking radars) and generates what we will refer to as "MS tails." Moreover, radiation that is scattered out from the field of view of the instrument (e.g., after the first scattering event in the example shown in Fig. 5) may be scattered back into it (e.g., at the third order of scattering). In presence of very strong attenuation such

contributions can actually overwhelm the SS signal. This mechanism is particularly important for systems with small footprints such as HIWRAP.

Dense ice particles are very efficient scatterers and do represent an optimal source of MS. The schematic in Fig. 5 depicts the effect of increasing MS contamination onto the reflectivity profiles measured from a platform overflying a cumulonimbus cloud similar to our observations. Such an increase of MS contributions can be achieved, for instance, by increasing either the ice content or the radar footprint, or both. Conversely, we assume the rain profile in the lower troposphere remains the same. The reflected signal measured at the receiver (continuous line) gradually departs from what is predicted from SS theory (dashed line). Whereas in the presence of weak MS, the shape of the profile remains quite similar to the SS one, moderate and strong MS contamination levels tend to significantly modify the reflectivity profile, especially in the rain portion (lower 5 km in the illustration), with the generation of MS tails characterized by low vertical reflectivity gradients and by a change in concavity. Since the MS tends to trigger at higher elevations for higher frequencies (because of the relatively higher scattering and extinction responses to small particles), such concavity causes the slope of $Z_{\mathrm{att,Ka}}$ to become less than $Z_{\mathrm{att,Ku}}$ as the profile extends downward; and therefore it can produce the DWR knee. Interestingly, the radar signal apparently coming from ranges close to the surface (which represents the key information for retrieving rain at the ground) can be completely decoupled from what is actually happening at such ranges. In regimes of strong MS, even the strong surface return can be masked by the MS tail. The disappearance of the surface peak has been documented in *CloudSat* observations (Battaglia and Simmer 2008) and in TRMM observations as well (S. Tanelli 2013, unpublished presentation at Precipitation Measuring Mission Science Team Meeting). In such cases MS has already been identified as the only plausible cause. Similarly, anomalous sloping has been observed in *CloudSat* data (Battaglia et al. 2010) and simulated for a *CloudSat*-like W-band radar (Matrosov et al. 2008).

The two salient features present in the HIWRAP observations therefore correspond to well-known signatures of the MS tail. What we hypothesize is that the convective core is producing a substantial attenuation in the form of scattering at both HIWRAP frequencies, so that the signals apparently coming from surface ranges and from ranges corresponding to the bottom part of the ''DWR leg'' (i.e., the portion of the profile below the knee) are not produced by a single backscattering event but rather are the result of MS events occurring higher up in the atmosphere.

The novelty of these HIWRAP observations consists in the occurrence of such phenomena at Ku band for an airborne configuration, which is known to disfavor MS effects due to smaller footprints (Battaglia et al. 2010), and the simultaneous availability of two frequencies (three, if we include also the collocated S-band ground-based polarimetric radar). This is the first time ever that evidence of MS is documented in dual-frequency observations (Ku and Ka). It is the scope of this paper to prove this hypothesis plausible and sensible for the HIWRAP case study under investigation.

a. Back to basics: MS pulse stretching

To understand the key parameters and variables affecting the MS signal a cylindrical geometry as depicted in Fig. 6 has been adopted. Two aspects are critical for the MS simulation: a proper radar antenna pattern (inclusive of sidelobes) and an explanation for the finite size of the convective cell. For the sake of simplicity we use a horizontally uniformly filled cylindrical convective cell. The radius of the convective cell will be indicated by r_{cc}. While in first approximation the antenna pattern for the Ku and Ka channels can be assumed to correspond to a main lobe (ml) with a Gaussian circular pattern with beamwidths of 3° and 1.2°, respectively, sidelobes (sl) are also evident in the measured antenna patterns (see the measured H and V cuts in Fig. 7). To include them we add to the Gaussian pattern a linear gain of the form $G_{\mathrm{sl}} = 10^{[-63.0-1.9\theta(^\circ)]/30.0}$ for the Ku and $G_{\mathrm{sl}} = 10^{[-2.0-10\theta(^\circ)]/10.0}$ for the Ka. A flat background value B_{sl} equal for all incoming directions is also included. Values of −40 and −30 dB are assumed as typical and seem to be representative of the HIWRAP antenna patterns (see black and red lines in Fig. 7). Note that $B_{\mathrm{sl}} = -30$ dB overestimates the measured sidelobes; however, note that the antenna patterns depicted in Fig. 7 have been measured before mounting HIWRAP on the airplane, and the sidelobes are believed to be more pronounced once the radar is mounted on the airplane. The simulation framework is applied to a three-layer profile, which is constituted by a uniform middle layer with thickness ΔH, characterized by a constant value of hail content distributed according to a gamma distribution and here characterized by the mass-weighted mean diameter D_m and its normalized standard deviation σ_N. The middle layer is surrounded by two 2-km-thick layers with hail water content and mass-weighted mean diameter linearly decreasing to zero (a schematic of such trapezoidal profile is sketched in the light yellow inset in Fig. 6). As a proof of concept, the results for a HIWRAP Ku configuration for a layer with hail water content (HWC) equal 2 g m^{-3}, ΔH = 4 km, and D_m = 10 mm are shown in Fig. 8a. Note that

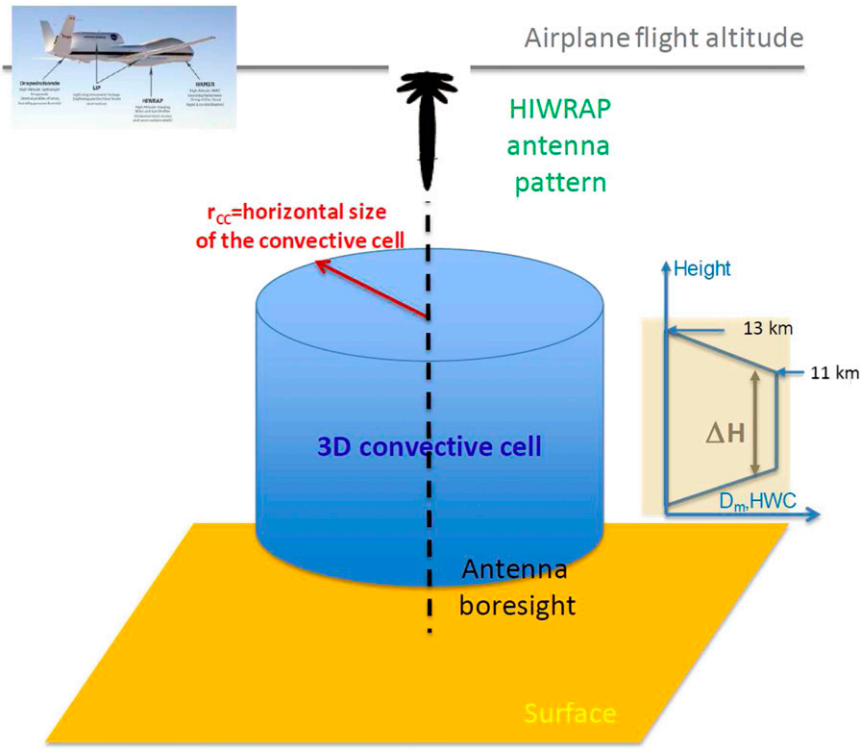

FIG. 6. Geometry of the MS simulations for the airborne configuration. The trapezoidal shape represents the model assumption for the vertical profile of the hail microphysics.

in this example no surface is introduced in the simulations (i.e., all returns are generated by atmospheric targets). All the MS curves (symbols) are clearly departing from the SS approximation (continuous black line) with the obvious introduction of considerable pulse stretching far beyond the bottom of the cloud (located at 3 km). MS profiles—especially those corresponding to r_{cc} = 10 km—are also characterized by a change of the concavity with an inflexion point located around the height where the higher-order scattering contributions

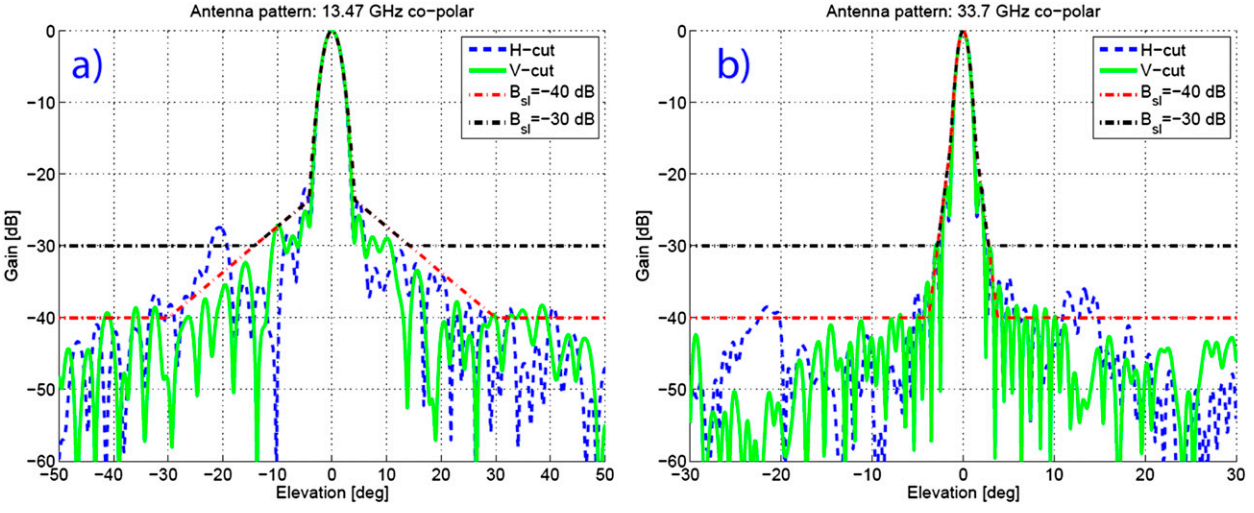

FIG. 7. Antenna patterns for the HIWRAP (a) Ku and (b) Ka bands. The measured *H* (*V*) cuts as measured by the antenna manufacturer are shown as dashed (dash-dotted) lines while the antenna patterns used in this study inclusive of main lobes and sidelobes are shown as dash-dotted red and black lines.

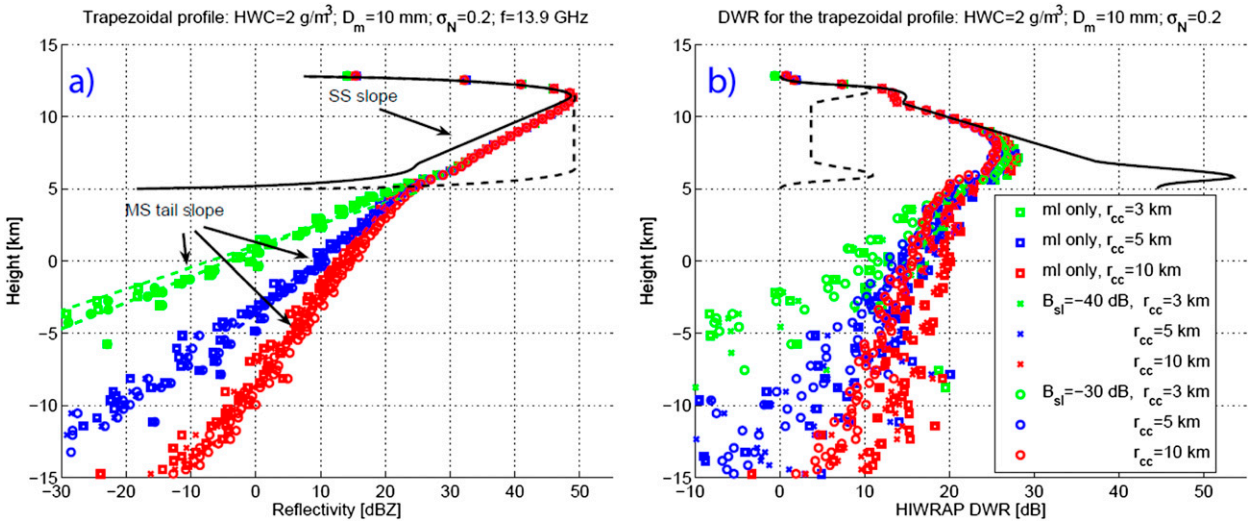

FIG. 8. (a) Example to demonstrate the tail effect introduced by MS at the Ku band for a trapezoidal profile with $\Delta H = 4$ km. (b) DWR for the profile shown in (a). The letters ml (sl) stand for main lobe (sidelobe). The black continuous (dashed) lines correspond to the SS attenuated (effective) profiles.

become predominant in the overall return. The amount of the MS enhancement and the slope of the reflectivity profiles within the region dominated by MS are a strong function of r_{cc} (different colors in Fig. 8). The details of the adopted antenna pattern (different symbols) are less important but not negligible, especially for the HIWRAP Ka system and, as a consequence, also for the DWR (Fig. 8b). Results of Fig. 8a are expected: MS is certainly enhanced for systems that have significant horizontal extension and with antennas with large sidelobe effects. Note that for this specific profile the SS total attenuation amounts to 30 dB (i.e., not enough to mask the surface return as occurring in feature 1). However, introducing additional attenuating hydrometeors below the hail scattering layer will ensure that the surface is masked without significantly modifying the reflectivity profile itself close to the surface bins. In such a situation the reflectivity profile will pass smoothly through the surface range (feature 1). The MS DWR clearly presents a nonmonotonic behavior and shows a behavior quite different from the SS DWR in the region where the signal is strongly affected by MS with a maximum value significantly lower than that found in the SS approximation. Note that because of the specific shape of the trapezoidal profile the SS DWR presents a knee clearly related to the decrease in size of the hail particles occurring between 7 and 5 km, but it is actually limited to an even shorter distance [~(6–5) km] because of the partially compensating effect of differential attenuation. The MS results seem to reproduce much better the behavior of the measurements (Fig. 2) with the decrease of DWR continuing for several kilometers below the height of maximum DWR. Furthermore, what is important is that, contrary to the SS simulations, many possible microphysical scenarios result in MS profiles that qualitatively capture the two salient features of interest in this dataset.

By spanning a variety of profiles with different thicknesses $\Delta H = 2$, 3, and 4 km, HWC between 0.5 and 3 g m^{-3}, and D_m between 5 and 30 mm, it is possible to study the relationship between the slope of the SS profile (due to attenuation) within the homogeneous layer and the slope of the MS tail, hereinafter defined as the mean slope in the 10-km-thick layer from the bottom of the ice layer downward (see arrows in Fig. 8a). Results are shown in Fig. 9a for the HIWRAP Ka channel slope but very similar results are found for the Ku channel. In general increasing the attenuation coefficient (i.e., the SS reflectivity slope) of the homogeneous layer (i.e., moving rightward on the x axis) has the effect of decreasing the slope of the MS tail (y axis), that is, of creating a longer pulse stretching that will potentially remain above the minimum detection threshold for longer ranges. For the HIWRAP Ka configuration it is clear that very large convective core systems (r_{cc} = 10 km, like the one observed during MC3E) can produce tail slopes as low as 1 dB km^{-1} already for SS reflectivity slopes on the order of 4–5 dB km^{-1} (which corresponds for instance to a hail content of 1 g m^{-3} and D_m around 6 mm). Generating tails with small slopes becomes increasingly difficult for small-scale convective systems (green symbols) and require extremely large SS reflectivity slopes (i.e., huge hail water content). At Ku we see a very similar behavior as at Ka, again with

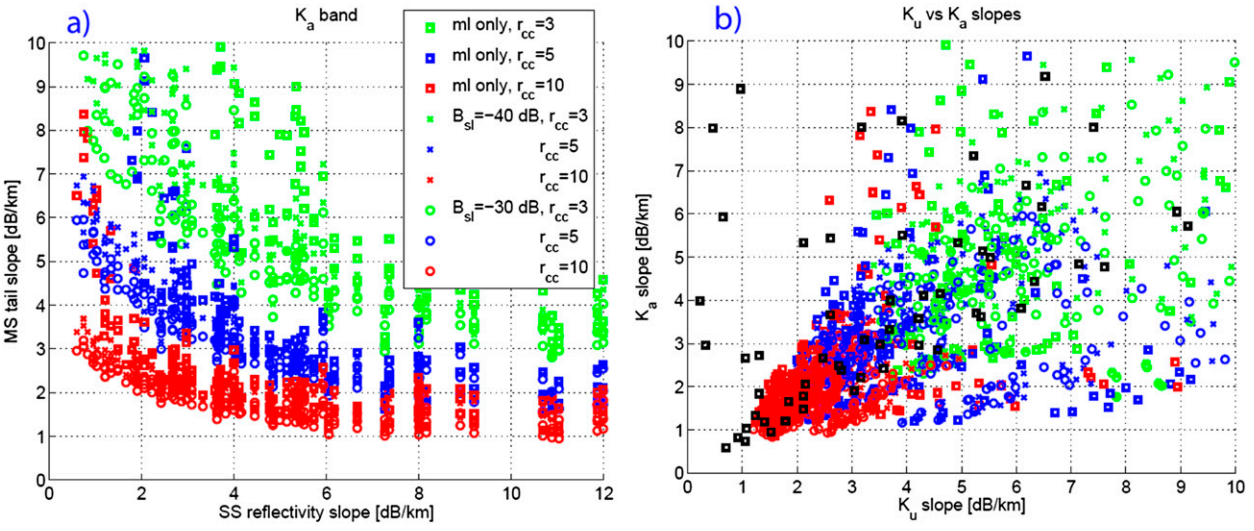

FIG. 9. (a) Slopes of the MS pulse-stretching tail as a function of the SS reflectivity slope (equivalent to the two-way attenuation coefficient) in the Ka band. (b) The Ku vs Ka slopes for the HIWRAP configuration. The legend is as in (a) with the black squares corresponding to SS.

a huge difference between small and large convective cores.

For all our simulations we have then compared the MS tail slopes for the two HIWRAP channels (Fig. 9b). As a reference we have also plotted the SS slopes (black squares). For very large convective systems (red symbols) the tail slopes seem to be all concentrated in a region with Ka slopes between 1 and 3 dB km^{-1} and never exceeding the corresponding Ku slope. Even when considering smaller systems the slope at Ka band seems always to be comparable to or larger than the corresponding slope at Ku. This is exactly the kind of feature that has been observed by the HIWRAP radar.

b. *Profiles compatible with HIWRAP observations*

Profiles with the simple trapezoidal shape and cylindrical symmetry presented in section 3a are sufficient to roughly explain the two salient features that we have highlighted in section 2a. Here we will apply the MS framework to more detailed microphysical structures to demonstrate that it can reproduce the observed profiles of reflectivity. By looking at the DWR profile (Fig. 1c) we have grouped the profiles in two clusters, one for along-track ranges centered at an along-track distance of 24 km (sector I) and the other at 31 km (sector II). The envelopes of the observed HIWRAP profiles within ±1, ±3, and ±5 km from the cluster center are depicted as gray-shaded areas with increasing brightness in Figs. 10a,b and 11a,b. Note that for sector I the Ka signal (see dark gray envelope in Fig. 10b) is hitting the noise level approximately at heights lower than about 4 km. The blue-shaded area corresponds to the envelope of observed S-band collocated profiles within ±3 km from the sector center.

The two sectors show some relevant differences. While the first sector is developing extremely high reflectivities at very high altitudes [e.g., S-band (Ku band) reflectivities exceeding 60 dBZ (47 dBZ) already at 12 km (14 km)], in the second sector Ku reflectivities are peaking at 10 km and S-band reflectivities are exceeding 60 dBZ only in the lower atmosphere. The first sector seems also to manifest more MS effects with two distinct tails at the two frequencies starting at about 9 and 11 km, respectively. In the second sector, on the other hand, the Ku band seems to have an anomalous sloping only in the last 2 km whereas the Ka tail seems to start at about 9 km.

Based on the observed triple-frequency profiles, we looked for hydrometeors profiles that are capable of explaining the observations. These profiles have been built heuristically in a top to bottom (surface) approach.

1) In the top part of the cloud the SS approximation is certainly valid. In that region the HIWRAP dual frequency observations can nicely constrain a single-mode particle distribution. The DWR first constrains the size of the particles while one of the two reflectivities is used to retrieve the hydrometeor content. Very soon [roughly below 15 (14) km for sector I (II)] significant attenuation is produced in the Ka channel (see departure between continuous and black lines in Figs. 10a,b and 11a,b).
2) Below 12 km, MS enhancement starts significantly affecting both the Ka and the Ku reflectivity profiles

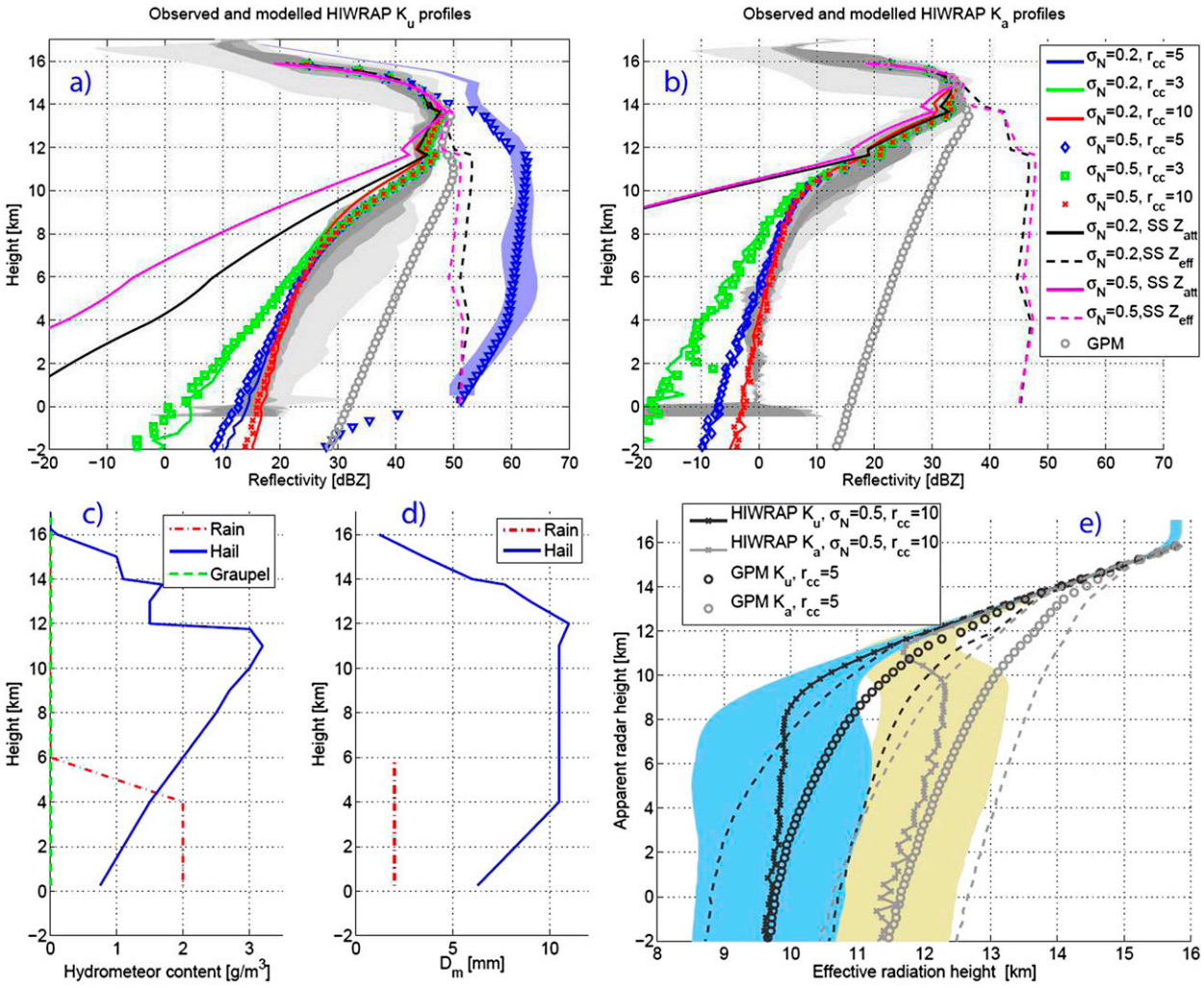

FIG. 10. Best-matched simulated profile for the observed HIWRAP (a) Ku and (b) Ka profiles from sector I corresponding to an along-track distance of 24 km in Fig. 1. Different configurations have been selected as shown in the legend. The different gray-shaded areas correspond to the envelope of observed profiles within ±1, ±3, and ±5 km from the sector center. The blue-shaded areas correspond to the envelope of observed S-band collocated profiles within ±3 km from the sector center while the blue triangles correspond to the simulated S-band profile. The gray lines made up of circles correspond to GPM observations with $r_{cc} = 5$ km and $\sigma_N = 0.5$. (c) Hydrometeor profiles corresponding to the best-matched reflectivity profiles shown in (a) and (b). (d) The D_m profiles corresponding to the hydrometeor profiles shown in (c). (e) Effective radiation height vs apparent radar bin height corresponding to the best-matched reflectivity profiles shown in (a) and (b); the gray lines correspond to the Ku (dark gray) and to the Ka (light gray) GPM simulations. The shaded areas (dashed lines) mark the 1-σ variability of the effective radiation height for HIWRAP (GPM) computed from the different trajectories simulated with the Monte Carlo method.

in both sectors. The retrieval problem becomes highly nonlocal and has been based on a trial-and-error approach. When using SS approximation, we always encountered problems in fitting simultaneously the three reflectivity profiles below 10 and 8 km for sectors I and II, respectively. On the other hand, with the MS approach, the main problem is that of ambiguity: many profiles can explain the observed profiles to a first approximation, and the fine details of the vertical structure can be adjusted to reproduce the finescale features.

3) Below 10 km (i.e., where the S-band vertical resolution is good enough) the ground-based S-band profile helps in constraining the large-particle mode. The problem is clearly underconditioned. After running several MS simulations with fine-tuned profiles we succeeded in getting simulated reflectivity profiles that are in agreement with the observed ones. As part of the fine tuning we found it necessary to introduce a second small mode (graupel) in the second sector to better reproduce the Ku reflectivity bump at about 8-km altitude, but indeed a similar result could be

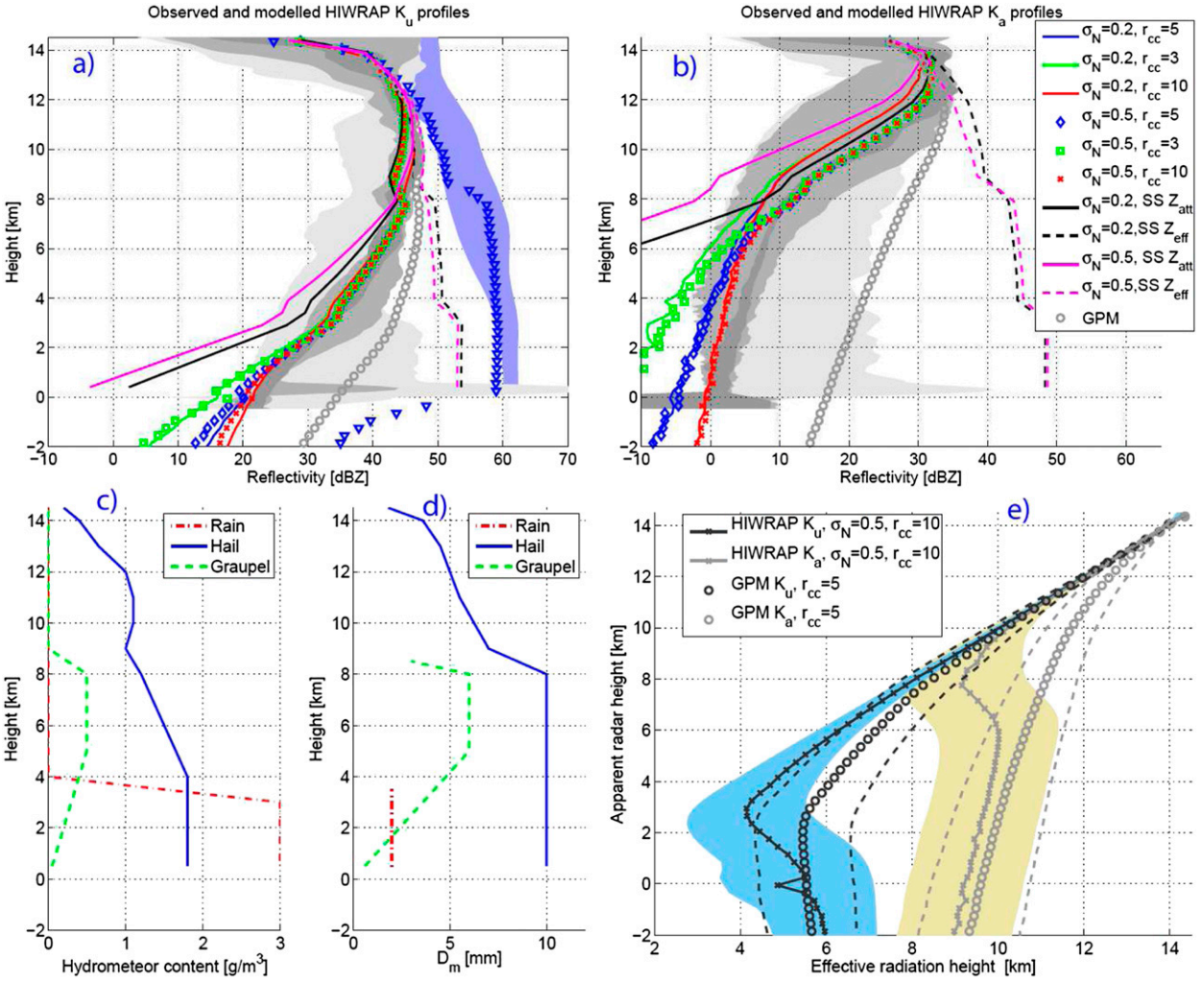

FIG. 11. As in Fig. 10, but for sector II centered at an along-track distance of 31 km as labeled in Fig. 1b.

achieved with other minority scatterers such as small hail, or a mix of liquid and solid scatterers. In general there is little information in regard to the lower portions of the structure other than it has to produce sufficient attenuation to suppress the surface return below the MS tail. Such attenuation can be associated with low albedo (rain), medium albedo (wet hail), or high albedo (dry hail), or a mix thereof: since any MS starting from these lower altitudes is already masked under the MS tail generated above, there is really no way to discern. Such distinction would require analysis, for example, of the horizontal map of S-band attenuation and reflectivity from the KUON PPI, but it is beyond the scope of this paper since it does not impact the Ku- and Ka-band profiles.

Microphysical profiles that roughly match both the HIWRAP and the S-band observations are shown in Figs. 10c,d and 11c,d. Both profiles are characterized by the presence of only moderate hailstones (with mass-weighted mean diameters up to 12 mm) and large hail ice contents (i.e., integrated contents exceeding 15 kg m^{-2}). Notably, larger sizes and contents are produced in spectral bin microphysics models (e.g., Ryzhkov et al. 2011). In sector II a large amount of hail is reaching the ground. This was confirmed by near-zero Z_{DR} near the surface and by S-band reflectivities exceeding 55 dBZ (Heymsfield et al. 2013). In sector I, the updraft is so strong (Fig. 1d) that large hail stay aloft.

Note that these profiles should not be intended as a deterministic retrieval; rather, they have to be considered only as a possible solution in the solution space. For such microphysical profiles, the simulated HIWRAP profiles corresponding to different σ_N and different r_{cc} values as indicated in the legend are plotted in the two top panels. Results fit quite well the observed HIWRAP

profiles; still, some difficulties remain in exactly matching the Ka tail at very low altitudes. Uncertainties in the 3D structure of the system and in the antenna pattern sidelobe details—two factors that can strongly affect such features—contribute to complicate the problem. The solution with r_{cc} =10 km (for all the plotted curves B_{sl} is equal to −35 and −30 dB at Ku and Ka, respectively) provides the closest matching in this case. For completeness, in Figs. 10a,b and 11a,b the reflectivity factor and attenuated reflectivity from single-scattering (labeled as SS Z_{att} and SS Z_{eff}) profiles (continuous and dashed lines) corresponding to σ_N = 0.2 (magenta curves) and σ_N = 0.5 (black curves) are plotted as well. Our results support the idea that, in sector I, not only the majority of the Ka but also a great part of the HIWRAP Ku profile is contaminated by MS; this is partially mitigated for sector II, especially for the Ku channel. This is further demonstrated by the behavior of the effective radiation height as a function of the apparent radar-bin height in Figs. 10e and 11e. The effective radiation height is defined as

$$\text{Effective radiation height}(r) \equiv \frac{\sum_k z_{\text{eff}}^{(k)} Z_{\text{att}}^{(k)}(z)}{\sum_k Z_{\text{att}}^{(k)}(z)}, \quad (5)$$

where the summation is performed over different trajectories stochastically simulated by Monte Carlo methods, contributing to the range bin at mean distance r; $Z_{att}^{(k)}$ is the contribution of the kth trajectory to the observed radar reflectivity while $z_{eff}^{(k)}$ indicates the mean height of all scattering events occurred during the kth trajectory. Figure 5 provides an example of two trajectories contributing to the same radar-bin height but different z_{eff}. Clearly for SS events z_{eff} coincides with the height at which the backscattering is occurring. The effective radiation height provides an indication of the height from where the returned power is generated. In Figs. 10e and 11e the departure from the 1-to-1 line mirrors the departure from the SS approximation. The shadings correspond to the one-sigma variability computed over an ensemble of possible trajectories. Not surprisingly in sector I all the radiation sensed by the radar, even at apparent radar heights close to the surface, corresponds to radiation mainly scattered above 8 km. Consequently the hydrometeor profiles in the low atmosphere are indeed affecting only the S-band signal, and the strength of the surface return at Ku and Ka band. With the only S-band constraint it is then quite simple to find many other profiles (by modifying the one here proposed in the lower troposphere) that fit the observations. However, only by fine-tuning the ice portion of the cloud (i.e., the part above 8 and 5 km for sectors I and II, respectively) can we trigger the right MS in the low troposphere and get (almost) the right slope for the Ku and the Ka, and hence of the DWR. It is out of the scope of this paper to provide a retrieval of the hydrometeor profiles within the convective core, as that would likely entail an analysis of the climatology from other sources so that one could correlate the upper portion of the storm to the lower portion.

Such considerations also confirm the doubts about the representativeness of the HIWRAP Doppler velocity measurements below such altitudes (Heymsfield et al. 2013) because of the major role played by MS [see Battaglia and Tanelli (2011) for a detailed description of MS effects on Doppler spectra]. The situation is somehow different in sector II but still the region below 2 km remains a "*hic sunt leones*" ("here be lions") region, that is, a region almost unexplored even by the Ku radiation transmitted by the radar.

Figure 12 shows DWR results as measured and simulated from MS and SS for the two sectors. Note that for sector I (Fig. 12a) at very low altitudes we do not get a perfect matching between simulations and observations (but note that at heights below 4 km the Ka channel is hitting the noise level), although we clearly capture the DWR "knee" behavior. As previously stated, details in the HIWRAP antenna pattern and the 3D structure of the storm may play a substantial role in affecting the Ka tail. Measurements with a more sensitive radar and a full characterization of the antenna pattern of the airborne-mounted system could possibly provide an even more accurate reproduction of the details of the observed profiles.

4. Effects expected for the GPM DPR observations

In correspondence to the same microphysical profiles shown in of Figs. 10c,d and 11c,d we have also simulated GPM observations with r_{cc} = 5 km and σ_N = 0.5 (gray circled lines in the top panels). MS is obviously much more pronounced in the GPM than in HIWRAP measurements because of its larger footprints. Amazingly the GPM DPR radar will provide a signal above its expected noise level for all ranges above surface for both sectors. The horizontal extent of the southern Great Plains hailstorms is often 10–20 km across and they are therefore likely to be detected by the GPM DPR with the 5-km GPM DPR spatial resolution.

To further investigate the potential effect of MS in GPM observations of hail-bearing convective cores the notional study performed in section 3a for the HIWRAP configuration has been repeated for the GPM-DPR configuration (400-km altitude; beamwidth of 0.7° both

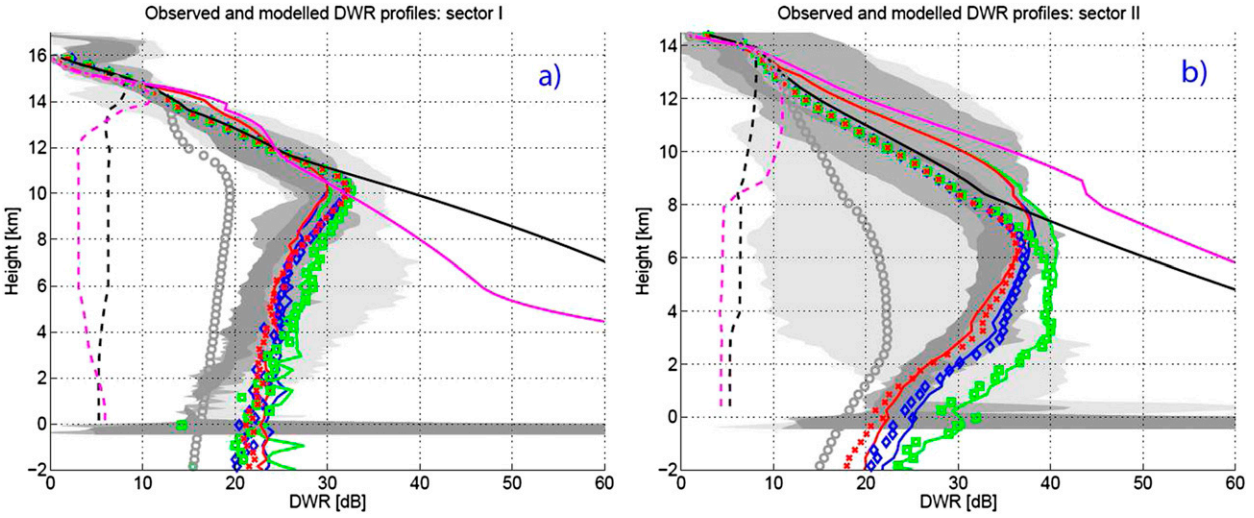

FIG. 12. DWR simulated and measured in correspondence to sectors (a) I and (b) II. The legend is as in previous figures. The gray lines with circles correspond to GPM simulations with $r_{cc} = 5$ km and $\sigma_N = 0.5$.

at Ku and Ka). An example of Ku and Ka reflectivities for HWC = 1.5 g m^{-3} and $D_m = 5$ mm and for $\Delta H = 2, 3, 4$ km are shown in Figs. 13a and 13b, respectively. The relevance of MS is obvious and it is also clear how the shape of the vertical reflectivity profile is affected by both the thickness of the ice layer (circle vs cross vs plus symbols) and by the horizontal extent of the system (blue vs green vs red). MS has a profound impact in the DWR profile as well, as demonstrated in Fig. 13c, with all MS profiles characterized by a knee shape. MS DWR values never exceed 20 dB at the maximum level but they may even become negative at the bottom of the leg. The SS profiles also present a DWR knee but, in this case, the knee is simply caused by Mie differential effects, that is, by the decrease in the size of the hail particle moving downward, which is characteristic of the bottom part of the trapezoidal-shaped profiles used in the simulation. Given the GPM minimum detection threshold (here assumed to be 16 dBZ for both channels), only part of the DWR profiles will be detectable (highlighted by the continuous lines). While the SS-DWR knee is not detectable, the MS knees are all well detectable. It is noticeable that, similar to what was observed in HIWRAP (Fig. 9b), the GPM Ka reflectivity slopes will tend to be comparable to or even smaller than the corresponding GPM Ku slopes (not shown).

Consequences and ways forward

The main goal of GPM mission is in surface precipitation estimation. It is clear that the impact of MS to the precipitation estimation at the surface will be important in deep convective systems. Since MS effects for GPM will strongly depend on the size and spatial structure of the storm and on the ice microphysics properly accounting for MS will be challenging.

In the case of strong MS (far right profile in Fig. 5), it is clear that the radar has completely lost its ranging, detecting, and estimating capability close to the surface. In such conditions also the path-integrated attenuation estimated from surface reference technique (Meneghini et al. 2004) will be erroneous (underestimated), as already observed in *CloudSat* observations (Battaglia et al. 2008). Rain rates at the ground can be only based on statistical inference.

When MS is weaker (far left and center profile in Fig. 5) the surface reference technique will still be applicable but MS will modify the slope of the reflectivity profiles, and thus the DWR—a key parameter in rain retrieval based on attenuation. To avoid biases in rainfall estimates, this effect must be included in retrieval algorithms. However, it is obvious that the presence of MS and of coexistent nonuniform beam-filling effects (Takahashi et al. 2006; Tanelli et al. 2012) will substantially complicate the interpretation of GPM measurements of convective cores.

The first goal that needs to be achieved, though, is that of understanding the nature of phenomenon and characterizing its main features so that it can be detected. It is envisioned that initially dubious profiles will simply be flagged to prevent erroneous conclusions based on SS algorithms. Ultimately approaches similar or alternative to the one adopted for the same correction in the *CloudSat* products should be developed to mitigate these effects and extend the range of retrievable conditions.

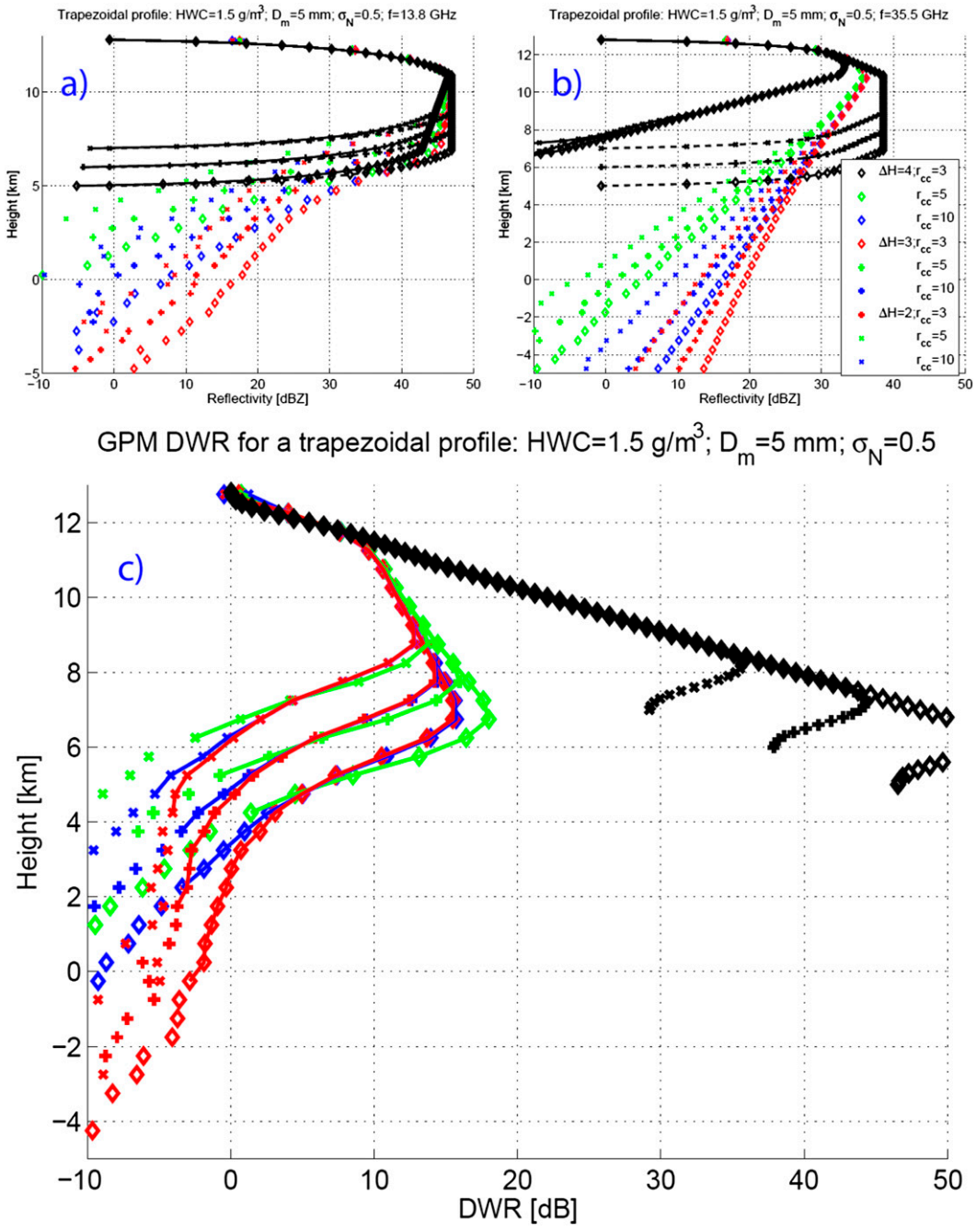

FIG. 13. GPM (a) Ku and (b) Ka vertical reflectivity profiles for a trapezoidal profile with HWC = 1.5 g m^{-3}, D_m = 5 mm, and σ_N = 0.5. Black corresponds to the simulated SS effective (symbols) and attenuated (continuous line plus symbols) reflectivities for ΔH = 2, 3, and 4 km. The colored lines correspond to MS reflectivities for different ΔH and r_{cc} as indicated in the legend. (c) GPM DWR corresponding to the profiles depicted in (a) and (b). The continuous lines correspond to signal that would be detectable by the GPM-DPR.

For this purpose we propose two different strategies.

1) Fast codes that account for MS effects [e.g., the one developed in Hogan and Battaglia (2008)] can be adopted as forward operators in the retrieval algorithm. A similar strategy has been adopted for the *CloudSat* rain-profiling algorithm (Haynes et al. 2009; Mitrescu et al. 2010). In this approach three-dimensional effects and the interplay between MS and nonuniform beam filling cannot be properly

accounted for (fast codes are inherently one-dimensional).

2) If a fully three-dimensional microphysical dataset representative of convective events becomes available it will be possible to run full 3D simulations of the GPM signal inclusive of MS and in the SS approximation. The profiles with and without relevant MS will be isolated based on simulated SS truth, and a principal component analysis applied to both populations. This will allow identifying MS markers. A real DPR profile can then be projected into these two bases. If the best match is found in the MS-affected dataset, the corresponding SS profile is extracted through the truth mapping between MS and SS. The simulated profiles will be clustered according to environmental conditions (e.g., freezing level height or surface temperature) and to precipitating system characteristics as derived by GPM observations (e.g., cloud-top height, maximum reflectivity in the ice phase, presence of a melting layer, or integrated attenuations). These clustering analyses will allow refining criteria for identifying MS contaminated profiles and the likely altitude where MS starts contributing significantly to total reflectivity (as done in the *CloudSat* rain-profile product; Battaglia et al. 2011).

5. Summary and conclusions

Novel HIWRAP Ku–Ka dual-frequency observations of a strong convective cell in Oklahoma provide new evidence of MS effects in extreme hail-bearing weather events. Previous analysis of the same convective cell and our notional simulations support the presence of large ice particles hailstones in the observed profiles. Solutions compatible with observations suggest columnar hail water contents exceeding $15\,\mathrm{kg\,m^{-2}}$ and mass-weighted mean diameters ranging up to 12 mm. Because of their very high single-scattering albedos, these particles are very effective sources of MS both at Ka and at Ku band. The following relevant conclusions can be drawn from our study.

1) Dense ice particles are very efficient scatterers both at Ku and at Ka. Because of Mie effects, with the same amount of ice mass, dense ice particles with sizes in the range between 10 and 20 mm (4 and 7 mm) are the most efficient in producing attenuation at Ku (Ka) band (Figs. 3a,c). Attenuation coefficients reach up to almost 2 and $5\,\mathrm{dB\,km^{-1}\,(g\,m^{-3})^{-1}}$, respectively, at the two bands. Larger hailstones are less efficient in producing attenuation and they produce an anomalous, that is, negative, but never exceeding $-1\,\mathrm{dB\,km^{-1}\,(g\,m^{-3})^{-1}}$, Ka–Ku differential attenuation for mass-weighted mean diameters in the range between 12 and 28 mm (Fig. 4a).
2) A Ka–Ku DWR knee is frequently associated with MS. This signature can be explained straightforwardly with the help of MS theory when simulations involving hail-bearing convective cores with large horizontal extents are performed. The increase of the DWR with height in the lower atmosphere is interpreted as the result of MS pulse stretching caused by the highly diffusive hail layer positioned high up in the atmosphere, with Ka MS typically exceeding that occurring in the Ku channel. The emergence of the MS tail in the lower atmosphere can be observed thanks to the profile large attenuation and to the good HIWRAP sensitivity (10 and 0 dBZ at 20 km for Ku and Ka, respectively).
3) The MS strength is a strong function of the horizontal extent of the system and this is especially true for airborne systems. In fact, within systems characterized by high SS albedos, lateral diffusion allows radiation to reenter the small footprint (whose 3-dB radius is on the order of 500 and 200 m for HIWRAP at 10-km distance for Ku and Ka, respectively) after being scattered away from it. This process is increasingly more efficient for systems that have larger horizontal extents.
4) Antenna pattern sidelobe details play an important role in shaping the pulse stretching MS tails in airborne observations. High levels of the sidelobes enhance the contributions of lateral diffusion. Approximating the antenna pattern simply with a main Gaussian lobe is not sufficient to explain the observed HIWRAP profiles within the Oklahoma case study convective core. This is particularly true for Ka observations.
5) The Ka radiation has significant problems in effectively penetrating strongly attenuating convective storms. In fact, because of MS enhancement, the observed reflectivity sloping typically remains below the SS expected slope. This helps in keeping the signal above the noise level at the price of losing the radar ranging capability. For the Oklahoma storm the effective radiation height very often significantly exceeds the range height, with differences as high as 13 km. This means, for instance, that the signal close to the surface is mainly affected by hydrometeors located well above the freezing level.
6) If MS effects are indeed present in the aircraft measurements, they are likely to be more pronounced in the spaceborne GPM DPR observations. Our notional study supports the idea that DWR knees will be observed by the GPM radar when overflying high-density ice shafts embedded in large convective systems and suggests that their explanation must

not be sought in differential attenuation or differential Mie effects but via MS effects. As such the DWR knee could potentially be used as an MS signature. Soon, with real GPM DPR data becoming available, we will be able to confirm or refute our conjecture.

Acknowledgments. A portion of this work was funded by the NCEO Mission Support. A portion of this work (Tanelli) was carried out at the Jet Propulsion Laboratory, California Institute of Technology, under a contract with the National Aeronautics and Space Administration. This work was carried for the GPM mission under the Precipitation Measurement Missions program; support by Dr. Ramesh Kakar is gratefully acknowledged. The work performed by the engineering team led by Michael Coon, Lihua Li, Matthew McLinden, and Martin Perrine at Goddard made the measurements possible.

REFERENCES

Battaglia, A., and C. Simmer, 2008: How does multiple scattering affect the spaceborne W-band radar measurements at ranges close to and crossing the sea-surface range? *IEEE Trans. Geosci. Remote Sens.,* **46,** 1644–1651, doi:10.1109/TGRS.2008.916085.

——, and S. Tanelli, 2011: DOMUS: Doppler Multiple-Scattering simulator. *IEEE Trans. Geosci. Remote Sens.,* **49,** 442–450, doi:10.1109/TGRS.2010.2052818.

——, M. O. Ajewole, and C. Simmer, 2006a: Evaluation of radar multiple-scattering effects from a GPM perspective. Part I: Model description and validation. *J. Appl. Meteor. Climatol.,* **45,** 1634–1647, doi:10.1175/JAM2424.1.

——, ——, and ——, 2006b: Evaluation of radar multiple-scattering effects from a GPM perspective. Part II: Model results. *J. Appl. Meteor. Climatol.,* **45,** 1648–1664, doi:10.1175/JAM2425.1.

——, ——, and ——, 2007: Evaluation of radar multiple scattering effects in *Cloudsat* configuration. *Atmos. Chem. Phys.,* **7,** 1719–1730, doi:10.5194/acp-7-1719-2007.

——, J. M. Haynes, T. L'Ecuyer, and C. Simmer, 2008: Identifying multiple-scattering affected profiles in *CloudSat* observations over the oceans. *J. Geophys. Res.,* **113,** D00A17, doi:10.1029/2008JD009960.

——, S. Tanelli, S. Kobayashi, D. Zrnic, R. J. Hogan, and C. Simmer, 2010: Multiple-scattering in radar systems: A review. *J. Quant. Spectrosc. Radiat. Transfer,* **111,** 917–947, doi:10.1016/j.jqsrt.2009.11.024.

——, T. Augustynek, S. Tanelli, and P. Kollias, 2011: Multiple scattering identification in spaceborne W-band radar measurements of deep convective cores. *J. Geophys. Res.,* **116,** D19201, doi:10.1029/2011JD016142.

Durden, S. L., S. Tanelli, and R. Meneghini, 2012: Using surface classification to improve surface reference technique over land. *Indian J. Radio Space Phys.,* **41,** 403–410. [Available online at http://nopr.niscair.res.in/handle/123456789/14748.]

Haynes, J. M., T. S. L'Ecuyer, G. L. Stephens, S. D. Miller, C. Mitrescu, N. B. Wood, and S. Tanelli, 2009: Rainfall retrieval over the ocean with spaceborne W-band radar. *J. Geophys. Res.,* **114,** D00A22, doi:10.1029/2008JD009973.

Heymsfield, G. M., L. Tian, L. Li, M. McLinden, and J. I. Cervantes, 2013: Airborne radar observations of severe hailstorms: Implications for future spaceborne radar. *J. Appl. Meteor. Climatol.,* **52,** 1851–1867, doi:10.1175/JAMC-D-12-0144.1.

Hogan, R. J., and A. Battaglia, 2008: Fast lidar and radar multiple-scattering models: Part II: Wide-angle scattering using the time-dependent two-stream approximation. *J. Atmos. Sci.,* **65,** 3636–3651, doi:10.1175/2008JAS2643.1.

Hou, A. Y., and Coauthors, 2014: The Global Precipitation Measurement (GPM) mission. *Bull. Amer. Meteor. Soc.,* **95,** 701–722, doi:10.1175/BAMS-D-13-00164.1.

Kneifel, S., M. S. Kulie, and R. Bennartz, 2011: A triple-frequency approach to retrieve microphysical snowfall parameters. *J. Geophys. Res.,* **116,** D11203, doi:10.1029/2010JD015430.

Kobayashi, S., S. Tanelli, and E. Im, 2005: Second-order multiple-scattering theory associated with backscattering enhancement for a millimeter wavelength weather radar with a finite beam width. *Radio Sci.,* **40,** RS6015, doi:10.1029/2004RS003219.

——, S. Ito, S. Tanelli, T. Oguchi, and E. Im, 2007: A time-dependent multiple scattering theory for a pulsed radar with a finite beam width. *Radio Sci.,* **4,** RS4001, doi:10.1029/2006RS003555.

Kummerow, C., W. Barnes, T. Kozu, J. Shiue, and J. Simpson, 1998: The Tropical Rainfall Measuring Mission (TRMM) sensor package. *J. Atmos. Oceanic Technol.,* **15,** 809–817, doi:10.1175/1520-0426(1998)015<0809:TTRMMT>2.0.CO;2.

Liu, C., E. J. Zipser, and S. W. Nesbitt, 2007: Global distribution of tropical deep convection: Different perspectives from TRMM infrared and radar data. *J. Climate,* **20,** 489–503, doi:10.1175/JCLI4023.1.

Loftus, A. M., 2012: A triple-moment bulk hail microphysics scheme to investigate the sensitivities of hail to aerosols. Ph.D. dissertation, Colorado State University, 418 pp. [Available online at http://hdl.handle.net/10217/67571.]

Luo, Z., G. Y. Liu, and G. L. Stephens, 2008: *CloudSat* adding new insight into tropical penetrating convection. *Geophys. Res. Lett.,* **35,** L19819, doi:10.1029/2008GL035330.

Matrosov, S. Y., 1993: Possibilities of cirrus particle sizing from dual-frequency radar measurements. *J. Geophys. Res.,* **98,** 20 675–20 683, doi:10.1029/93JD02335.

——, A. J. Heymsfield, and Z. Wang, 2005: Dual-frequency radar ratio of nonspherical atmospheric hydrometeors. *Geophys. Res. Lett.,* **32,** L13816, doi:10.1029/2005GL023210.

——, A. Battaglia, and P. Rodriguez, 2008: Effects of multiple scattering on attenuation-based retrievals of stratiform rainfall from *CloudSat*. *J. Atmos. Oceanic Technol.,* **25,** 2199–2208, doi:10.1175/2008JTECHA1095.1.

Meneghini, R., and T. Kozu, 1990: *Spaceborne Weather Radar.* Artech House, 212 pp.

——, J. A. Jones, T. Iguchi, K. Okamoto, and J. Kwiatkowski, 2004: A hybrid surface reference technique and its application to the TRMM precipitation radar. *J. Atmos. Oceanic Technol.,* **21,** 1645–1658, doi:10.1175/JTECH1664.1.

Mitrescu, C., T. L'Ecuyer, J. Haynes, S. Miller, and J. Turk, 2010: *CloudSat* precipitation profiling algorithm—Model description. *J. Appl. Meteor. Climatol.,* **49,** 991–1003, doi:10.1175/2009JAMC2181.1.

Ryzhkov, A., M. Pinsky, A. Pokrovsky, and A. Khain, 2011: Polarimetric radar observation operator for a cloud model with spectral microphysics. *J. Appl. Meteor. Climatol.,* **50,** 873–894, doi:10.1175/2010JAMC2363.1

——, M. R. Kumjian, S. M. Ganson, and A. P. Khain, 2013: Polarimetric radar characteristics of melting hail. Part I:

Theoretical simulations using spectral microphysical modeling. *J. Appl. Meteor. Climatol.,* **52,** 2849–2870, doi:10.1175/JAMC-D-13-073.1.

Takahashi, N., H. Hanado, and T. Iguchi, 2006: Estimation of path-integrated attenuation and its nonuniformity from TRMM/PR range profile data. *IEEE Trans. Geosci. Remote Sens.,* **44,** 3276–3283, doi:10.1109/TGRS.2006.876295.

Tanelli, S., S. L. Durden, E. Im, K. S. Pak, D. G. Reinke, P. Partain, J. M. Haynes, and R. T. Marchand, 2008: *CloudSat*'s cloud profiling radar after two years in orbit: Performance, calibration, and processing. *IEEE Trans. Geosci. Remote Sens.,* **46,** 3560–3573, doi:10.1109/TGRS.2008.2002030.

——, G. F. Sacco, S. L. Durden, and Z. S. Haddad, 2012: Impact of non-uniform beam filling on spaceborne cloud and precipitation radar retrieval algorithms. *Remote Sensing of the Atmosphere, Clouds, and Precipitation IV,* T. Hayasaki, K. Nakamura, and E. Im, Eds., International Society for Optical Engineering (SPIE Proceedings, Vol. 8523), 852308-1–852308-9, doi:10.1117/12.977375.

Tian, L., G. M. Heymsfield, and R. C. Srivastava, 2002: Measurements of attenuation with airborne and ground-based radar in convective storms over land and its microphysical implications. *J. Appl. Meteor.,* **41,** 716–733, doi:10.1175/1520-0450(2002)041<0716:MOAWAA>2.0.CO;2.